

DESY 03-162
ITEP-LAT/2002-28
KANAZAWA-03-07

Dynamics of Monopoles and Flux Tubes in Two-Flavor Dynamical QCD

V.G. Bornyakov^{a,b,c}, H. Ichie^{d 1}, Y. Koma^{a 2}, Y. Mori^a,
Y. Nakamura^a, D. Pleiter^e, M.I. Polikarpov^c, G. Schierholz^{e,f},
T. Streuer^{e,g}, H. Stüben^h and T. Suzuki^a

– DIK *Collaboration* –

^a*Institute for Theoretical Physics, Kanazawa University, Kanazawa 920-1192,
Japan*

^b*Institute for High Energy Physics IHEP, RU-142284 Protvino, Russia*

^c*Institute of Theoretical and Experimental Physics ITEP, RU-117259 Moscow,
Russia*

^d*Institut für Physik, Humboldt-Universität zu Berlin, D-10115 Berlin, Germany*

^e*John von Neumann-Institut für Computing NIC,
Deutsches Elektronen-Synchrotron DESY, D-15738 Zeuthen, Germany*

^f*Deutsches Elektronen-Synchrotron DESY, D-22603 Hamburg, Germany*

^g*Institut für Theoretische Physik, Freie Universität Berlin, D-14196 Berlin,
Germany*

^h*Konrad-Zuse-Zentrum für Informationstechnik Berlin ZIB, D-14195 Berlin,
Germany*

Abstract

We investigate the confining properties of the QCD vacuum with $N_f = 2$ flavors of dynamical quarks, and compare the results with the properties of the quenched theory. We use non-perturbatively $\mathcal{O}(a)$ improved Wilson fermions to keep cut-off effects small. We focus on color magnetic monopoles. Among the quantities we study are the monopole density and the monopole screening length, the static potential and the profile of the color electric flux tube. We furthermore derive the low-energy effective monopole action. Marked differences between the quenched and dynamical vacuum are found.

¹ Present address: Institute for Theoretical Physics, Kanazawa University, Kanazawa 920-1192, Japan

² Present address: Max-Planck-Institut für Physik, D-80805 München, Germany

1 Introduction

The dynamics of the QCD vacuum, and color confinement in particular, becomes more transparent and amenable to quantitative investigation in the maximally abelian gauge (MAG) [1,2]. In this gauge the relevant degrees of freedom are color electric charges, color magnetic monopoles, ‘photons’ and ‘gluons’ [3]. The latter appear to become massive [4,5] due to a yet unresolved mechanism, resulting in an abelian effective theory at large distances. There is evidence that the monopoles condense in the low temperature phase of the theory [2,6], causing a dual Meissner effect which constricts the color electric fields into flux tubes, in accord with the dual superconductor picture of confinement.

The dynamics of monopoles has been studied in detail in quenched lattice simulations. It turns out that in the MAG the string tension is accounted for almost entirely by the monopole part of the abelian projected gauge field [7,8], and that the low-energy effective monopole action is able to reproduce both the string tension and the low-lying glueball masses [9]. Furthermore, many of the non-perturbative features of the vacuum, such as the topological charge density [10,11,12] and spontaneous chiral symmetry breaking [13], can be traced back to monopole excitations.

Very little is known about the dynamics of monopoles in the full theory. So far the investigations have concentrated mainly on the static potential. While the effect of sea quarks is clearly visible at short distances, even for relatively heavy quark masses [14,15,16], no significant changes have been observed in the long-range behavior of the potential and the string tension. In contrast, the critical temperature of the chiral phase transition was found to depend noticeably on the mass of the dynamical quarks [17,18,19], which indicates that sea quarks have a visible effect on the non-perturbative properties of the vacuum as well.

It will be interesting now to see how the microscopic properties of the vacuum react to the introduction of dynamical color electric charges. In this paper we shall study the effect of sea quarks on the dynamics of monopoles and the confining potential, and on the effective monopole action. The paper is organized as follows. In Section 2 we present the details of our simulations, as well as the gauge fixing procedure and abelian projection. In Section 3 we discuss the gross properties of the vacuum, such as the monopole density and the magnetic screening length, and the static potential. Furthermore, the problem of Gribov copies is addressed. Section 4 is devoted to a detailed study of the static and dynamical properties of the color electric flux tube. In Section 5 we derive the effective monopole action, employing an extended Swendsen method [20]. Finally, in Section 6 we conclude. Preliminary results of this work have been reported in Ref. [21].

2 Simulation details

Our studies are based on gauge field configurations with $N_f = 2$ flavors of dynamical quarks generated by the QCDSF–UKQCD collaboration, using the Wilson gauge field action and non-perturbatively $O(a)$ improved Wilson fermions [22]:

$$S_F = S_F^{(0)} - \frac{i}{2} \kappa g c_{SW} a^5 \sum_s \bar{\psi}(s) \sigma_{\mu\nu} F_{\mu\nu}(s) \psi(s), \quad (1)$$

where $S_F^{(0)}$ is the ordinary Wilson fermion action. Our data sample and run parameters are listed in Table 1. We will compare the results with the outcome of quenched simulations on lattices of similar size and lattice spacing. The parameters of our quenched runs are also given in Table 1.

We fix the MAG [25] by maximizing the functional

$$F[U] = \frac{1}{12V} \sum_{s,\mu} (|U_{11}(s, \mu)|^2 + |U_{22}(s, \mu)|^2 + |U_{33}(s, \mu)|^2) \quad (2)$$

with respect to local gauge transformations g of the lattice gauge field,

$$U(s, \mu) \rightarrow U^g(s, \mu) = g(s)^\dagger U(s, \mu) g(s + \hat{\mu}). \quad (3)$$

To do so, we use a simulated annealing (SA) algorithm [26], in which the gauge transformed link variables U^g are thermalized according to the probability distribution

$$p(U^g) = \exp\{F[U^g]/T\}, \quad (4)$$

where T is an auxiliary ‘temperature’ which is gradually decreased after every Monte Carlo sweep from $T = 5$ to $T = 0.04$. To do so, we use 7500 sweeps on the $16^3 32$ lattice and 10000 sweeps on the $24^3 48$ lattice. Every sweep consists of a heat bath update of each of the three $SU(2)$ subgroups of the link matrices. After the final temperature has been reached, several local gauge transformations are applied until $F[U]$ has attained its maximum value within machine precision. It is known [27,8] that the MAG is plagued by Gribov copies. This shows in the occurrence of local maxima of $F[U]$. As a result, gauge non-invariant observables will, in general, depend on how close one gets to the global maximum. Although the SA algorithm performs much better than the iterative local maximization procedure used in $SU(3)$ gauge theory so far, it is not always able to find the global maximum. We shall estimate the systematic error due to this problem in Section 3.

The functional $F[U]$ is invariant under local $U(1) \times U(1)$ gauge transformations and global Weyl transformations. From the (gauge fixed) $SU(3)$ link variables we derive abelian link variables [2,28]

$$u(s, \mu) \equiv \text{diag}(u_1(s, \mu), u_2(s, \mu), u_3(s, \mu)), \quad u_i(s, \mu) = \exp(i\theta_i(s, \mu)) \quad (5)$$

$N_f = 2$						
β	Volume	κ	c_{SW}	m_π/m_ρ	r_0/a	a [fm]
5.20	$16^3 32$	0.1355	2.0171	0.6014(73)	5.04(4)	0.0972(8)
5.25	$24^3 48$	0.13575	1.9603	0.6012(73)	5.49(3)	0.0911(5)
5.29	$24^3 48$	0.1355	1.9192	0.7029(49)	5.57(2)	0.0898(3)
5.29	$16^3 32$	0.135	1.9192	0.7586(22)	5.24(4)	0.0954(7)
5.29	$16^3 32$	0.134	1.9192	0.8311(26)	4.81(5)	0.104(1)
$N_f = 0$						
β	Volume				r_0/a	a [fm]
5.8	$24^3 48$				3.67	0.137(2)
6.0	$16^3 32$				5.37	0.091(1)
6.0	$24^3 48$				5.37	0.091(1)
6.2	$24^3 48$				7.38	0.068(2)

Table 1

Parameter values of our dynamical ($N_f = 2$) [22] and quenched ($N_f = 0$) gauge field configurations. The improvement coefficient c_{SW} was computed in [23]. The quenched r_0/a values have been taken from [24]. We have used $r_0 = 0.5$ fm to set the scale.

with

$$\theta_i(s, \mu) = \arg(U_{ii}(s, \mu)) - \frac{1}{3} \sum_{j=1}^3 \arg(U_{jj}(s, \mu)) \Big|_{\text{mod } 2\pi} \in \left[-\frac{4}{3}\pi, \frac{4}{3}\pi\right]. \quad (6)$$

The abelian link variables $u(s, \mu)$ take values in $U(1) \times U(1)$. Under a general gauge transformation they transform as

$$u(s, \mu) \rightarrow d(s)^\dagger u(s, \mu) d(s + \hat{\mu}), \quad (7)$$

$$d(s) = \text{diag}\left(\exp(i\alpha_1(s)), \exp(i\alpha_2(s)), \exp(-i(\alpha_1(s) + \alpha_2(s)))\right).$$

The monopole currents reside on links of the dual lattice and are defined by

$$k_i(*s, \mu) = \frac{1}{2\pi} \sum_{\square \in \partial f(s + \hat{\mu}, \mu)} \arg(u_i(\square)) = 0, \pm 1, \pm 2, \quad (8)$$

where $u_i(\square)$ is the product of abelian parallel transporters around the plaquette \square , and $f(s + \hat{\mu}, \mu)$ is the elementary cube perpendicular to the μ -direction with origin $s + \hat{\mu}$, with \square inheriting its orientation from $\partial f(s + \hat{\mu}, \mu)$. (Note that we differ here from the original and correct normalization of the monopole

currents [3].) The phases are chosen such that

$$\sum_i \arg(u_i(\square)) = 0 \quad |\arg(u_i(\square)) - \arg(u_j(\square))| \leq 2\pi. \quad (9)$$

Because of that,

$$\sum_{i=1}^3 k_i(*s, \mu) = 0. \quad (10)$$

3 Gross properties of the vacuum and static potential

Let us first look at the global changes of the QCD vacuum upon introducing dynamical color charges. Our smallest quark masses are of the order of the strange quark mass.

Monopole density

The monopole currents, which are conserved, form clusters of closed loops on the dual lattice. In case of the pure $SU(2)$ gauge theory it was observed that these clusters fall into two different classes [29,30]: ‘small’ (ultraviolet) clusters which are of limited extent in lattice units, and ‘large’ (infrared) clusters which percolate through the lattice and typically wrap around the boundaries. If the size of the lattice is large enough, a gap opens between the small and the large clusters, clearly separating the two. In general, each configuration accommodates at least one large cluster [30]. In Fig. 1 we show the histogram $h(L)$ of monopole currents of length L on the $24^3 48$ lattice. We observe two distinct clusters. For comparison we show the same quantity on the $16^3 32$ lattice in Fig. 2. Both lattices have a similar lattice spacing and quark mass. On the smaller volume no gap is observed. For the long-distance properties of the vacuum all what matters is the existence of long, percolating monopole loops. Whether they combine to one cluster or not is of secondary importance.

On smaller lattices we call a monopole cluster infrared if it forms the largest cluster or if the monopole loop wraps around the boundary. It has been shown in the pure $SU(2)$ gauge theory [31] that the corresponding monopole density does not depend on the lattice volume and scales properly, while the total monopole density diverges in the continuum limit.

We define the monopole density by

$$\rho = \frac{1}{12V} \sum_i \sum_{s,\mu} |k_i(*s, \mu)|. \quad (11)$$

In Fig. 3 we show the total monopole density as well as the density of monopoles belonging to the infrared cluster. In the former case the sum over s, μ extends

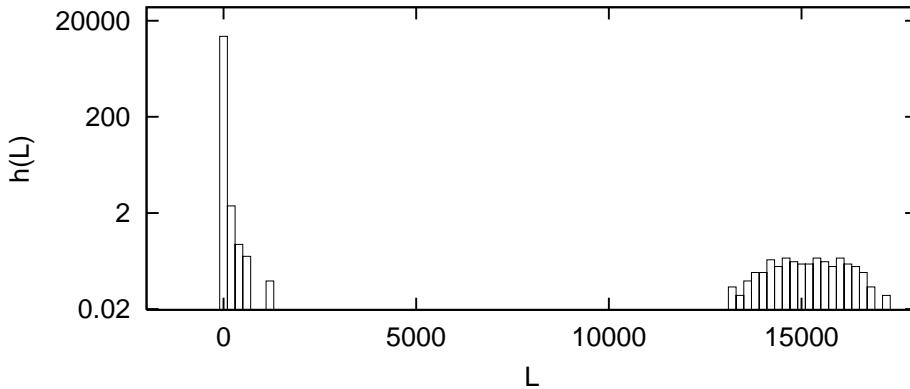


Fig. 1. The histogram of closed monopole loops of length L in full QCD on the $24^3 48$ lattice at $\beta = 5.29$, $\kappa = 0.1355$. The bin size is 200.

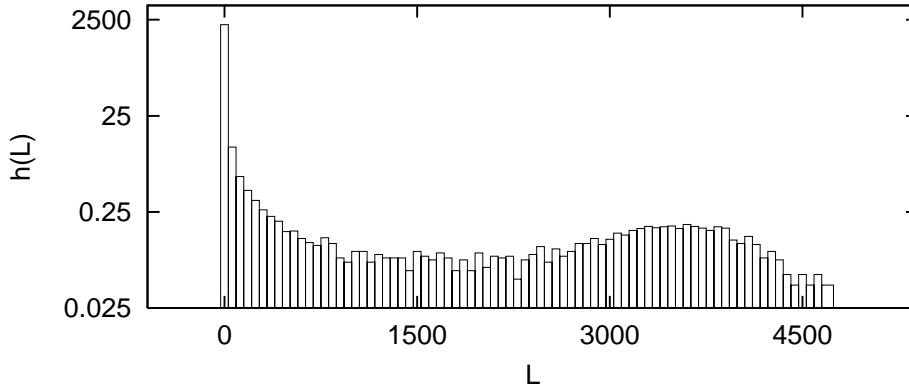


Fig. 2. The same as in Fig. 1, but on the $16^3 32$ lattice at $\beta = 5.29$, $\kappa = 0.135$. The bin size is 60.

over the full lattice, while in the latter case it extends over the links of the infrared clusters only. The quenched result is entered at $m_\pi/m_\rho = 1$. In the dynamical vacuum both densities are about a factor of two larger than in the quenched case. The total monopole density appears to increase with decreasing quark mass, while the density of infrared monopoles shows little variation, apart from the initial jump.

How can one explain the increase of the monopole density in the dynamical vacuum? It has been known for some time that monopoles are induced by (anti-)instantons [10,11], at least partially. The fermion determinant introduces an attraction between instantons and anti-instantons, and the force increases with decreasing quark mass [32]. The effect is, very likely, that the vacuum becomes solidly packed with instantons and anti-instantons, while isolated instantons are suppressed. As a result the density of (anti-)instantons

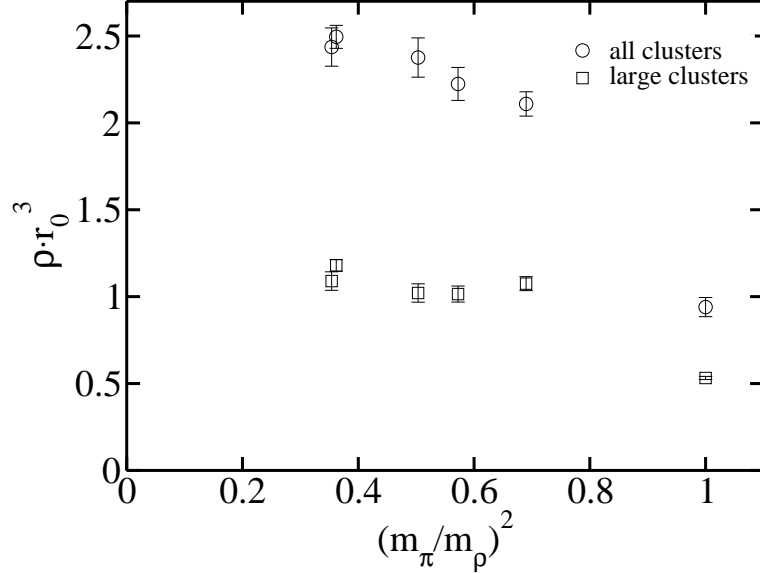


Fig. 3. The monopole density in full and quenched QCD. The quenched results refer to $\beta = 6.0$ and are listed at $m_\pi/m_\rho = 1$.

increases, and consequently the density of monopoles.

One should be aware that the total monopole density is not universal but depends, in general, on the action chosen, and that after integrating out the fermions the effective gluonic action may be more noisy than the Wilson gauge field action at the same lattice spacing. This would mainly affect the total monopole density, and to a lesser extent the infrared cluster.

Static potential

From the abelian projected link variables $u_i(s, \mu)$ we extract the abelian static quark-antiquark-potential. In order to improve the overlap with the ground state, we smear the space-like links according to

$$u_i(s, j) \rightarrow \alpha u_i(s, j) + \sum_{k \neq j} u_i(s, k) u_i(s + \hat{k}, j) u_i(s + \hat{j}, k)^\dagger. \quad (12)$$

We apply 30 smearing sweeps with $\alpha = 2$. The abelian potential $V_{\text{ab}}(R)$ is given by

$$V_{\text{ab}}(R) = \lim_{T \rightarrow \infty} \log \left(\frac{\langle W_{\text{ab}}(R, T) \rangle}{\langle W_{\text{ab}}(R, T+1) \rangle} \right), \quad (13)$$

where

$$W_{\text{ab}}(R, T) = \frac{1}{3} \text{Re Tr } \mathcal{W}_{\mathcal{C}}, \quad \mathcal{W}_{\mathcal{C}} = \prod_{s, \mu \in \mathcal{C}} u(s, \mu), \quad (14)$$

and \mathcal{C} is a (orientated) loop of spatial extent R and temporal extent T .

The ratio on the r.h.s. of (13) reaches a plateau at $T = 5$, so that we will

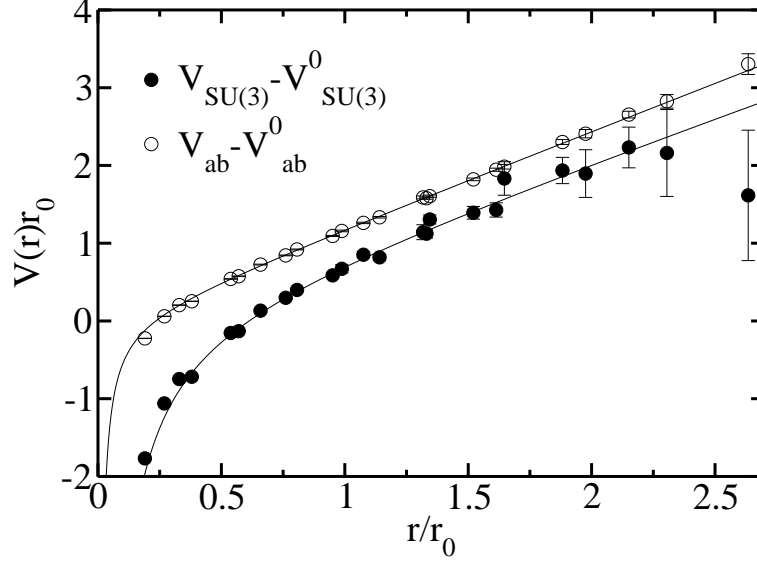


Fig. 4. Comparison of the abelian and non-abelian potential in full QCD on the $16^3 32$ lattice at $\beta = 5.29$, $\kappa = 0.135$. The solid lines are fits of the form (15).

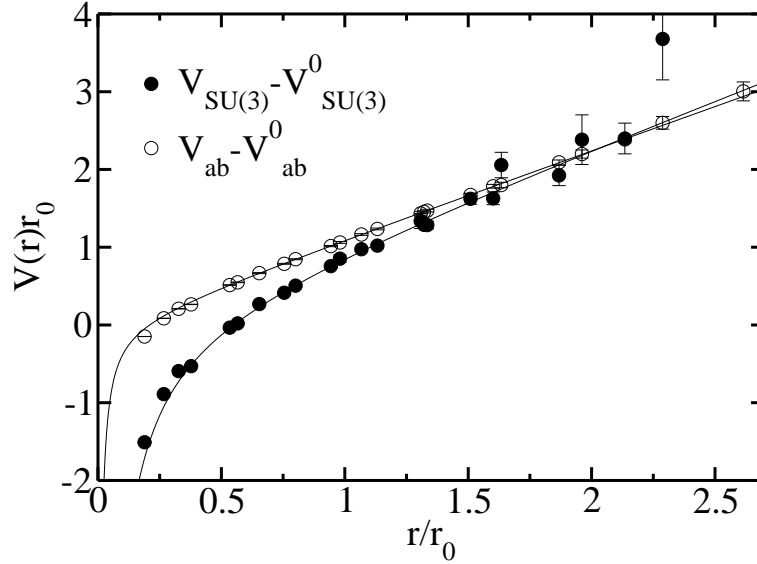


Fig. 5. Same as in Fig. 5, but for the quenched theory at $\beta = 6.0$.

take $T = 5$ throughout this section. We fit $V_{\text{ab}}(r)$ by the ansatz

$$V_{\text{ab}}(r) = V_{\text{ab}}^0 + \sigma_{\text{ab}} r - \frac{\alpha_{\text{ab}}}{r}. \quad (15)$$

The potential was calculated for on-axis and off-axis directions $\hat{r} = 1/\sqrt{2}(1, 1, 0)$ and $1/\sqrt{3}(1, 1, 1)$. At small r rotational symmetry is broken on the lattice, and we exclude the first four data points from our fits. The non-abelian static po-

m_π/m_ρ	α_{ab}	$\sigma_{\text{ab}}/\sigma$	$\sigma_{\text{mon}}/\sigma_{\text{ab}}$	ξ/r_0	$\sigma_{\text{ab}}/\rho\xi$
0.6014(73)	0.12(1)	0.90(4)	0.80(4)	0.484(19)	2.1(2)
0.7029(49)	0.10(1)	0.96(3)	0.87(3)	0.466(26)	2.6(3)
0.7586(22)	0.11(1)	0.99(6)	0.83(8)	0.521(17)	2.3(2)
0.8311(26)	0.11(1)	0.99(6)	0.88(5)	0.482(17)	2.5(2)
1	0.09(1)	0.83(3)	0.84(3)	0.662(34)	3.2(3)

Table 2

The Coulomb term, the abelian and monopole part of the string tension, as well as the monopole screening length in full and quenched QCD. The quenched result is shown in the last row and refers to the $16^3 32$ lattice at $\beta = 6.0$.

tential was extracted from the non-abelian Wilson loop using a corresponding procedure.

In Figs. 4 and 5 we show the abelian and non-abelian static potential for some data set. The self-energy contributions have been subtracted. The ratios of abelian and non-abelian string tensions are given in Table 2. As our determination of the non-abelian string tension was not accurate enough, we took these numbers from the literature: $\sqrt{\sigma}r_0 = 1.142(5)$ in full QCD [33] ($\sqrt{\sigma}r_0$ depends only weakly on the dynamical quark mass) and $\sqrt{\sigma}r_0 = 1.16(1)$ in the quenched theory [34]. The abelian string tension turns out to be very close to the non-abelian one in full QCD, while in the quenched case it is noticeably smaller. But the ratio of σ_{ab} to σ may increase in the continuum limit [31].

The abelian link variables can be decomposed into a ‘singular’ monopole part and a photon part according to the definition [35,36]:

$$\theta_i(s, \mu) = \theta_i^{\text{mon}}(s, \mu) + \theta_i^{\text{ph}}(s, \mu), \quad (16)$$

$$\theta_i^{\text{mon}}(s, \mu) = 2\pi \sum_{s'} D(s - s') \nabla_\alpha^{(-)} m_i(s', \alpha, \mu), \quad (17)$$

where $D(s) = \Delta^{-1}(s)$ is the lattice Coulomb propagator, $\nabla_\mu^{(-)}$ is the lattice backward derivative, and $m_i(s, \mu, \nu)$ counts the number of Dirac strings piercing the plaquette

$$u_i(s, \mu, \nu) = u_i(s, \mu) u_i(s + \hat{\mu}, \nu) u_i^\dagger(s + \hat{\nu}, \mu) u_i^\dagger(s, \nu). \quad (18)$$

If one computes $k_i(*s, \mu)$ from $\theta_i^{\text{mon}}(s, \mu)$ one recovers almost all monopole currents found by the definition (8), hence the notation monopole part [13].

Similarly, from Wilson loops composed of the monopole (photon) part of the link variables one can derive the monopole (photon) contribution to the static abelian potential. In Figs. 6 and 7 we show both contributions. The string tension of the monopole part σ_{mon} is given in Table 2, while the photon

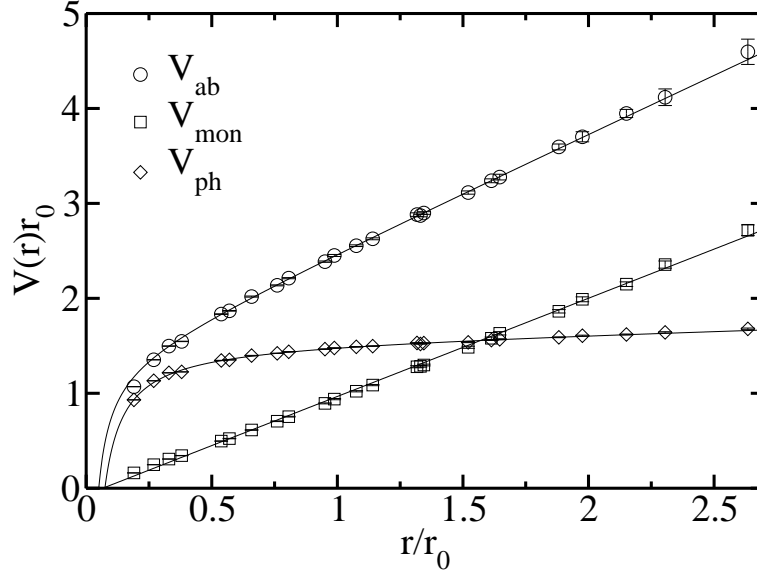


Fig. 6. Decomposition of the abelian potential into monopole and photon parts on the $16^3 32$ lattice at $\beta = 5.29$, $\kappa = 0.135$ in full QCD. The solid lines are fits of the form (15).

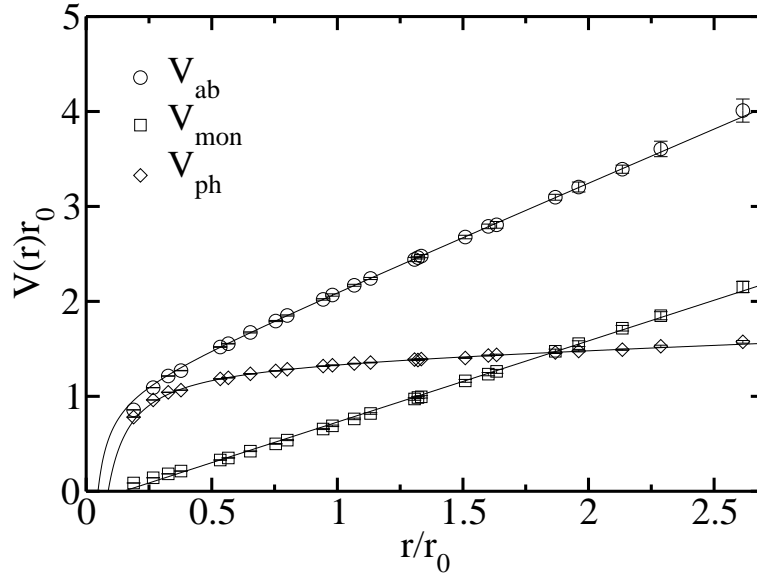


Fig. 7. The same as in Fig. 6, but for the quenched theory at $\beta = 6.0$.

contribution to the potential is short-range. Within the uncertainties (of $O(a^2)$ corrections) all string tensions are very similar, in the dynamical as well as in the quenched theory.

The next quantity we looked at is the magnetic screening length ξ . This is defined by the exponential decay of the magnetic flux $\Phi(r)$ through a sphere

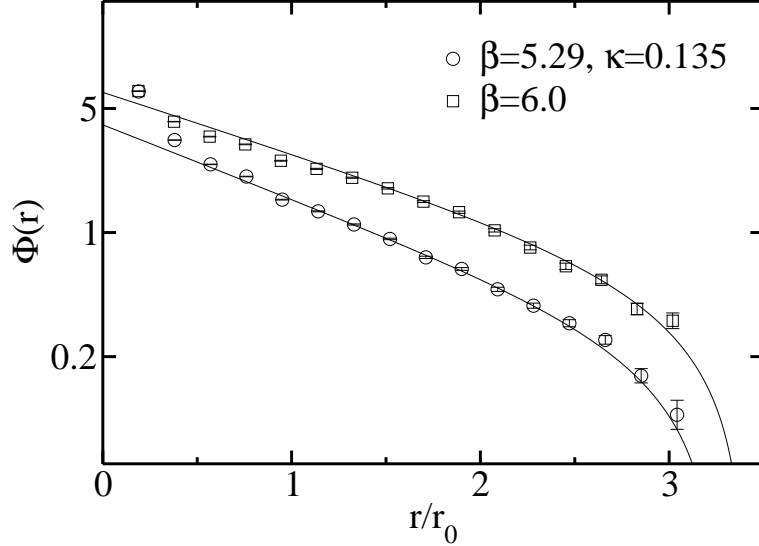


Fig. 8. Data and fit of the magnetic flux on the $16^3 32$ lattice in full and quenched QCD.

of radius r around the monopole. On a periodic lattice this can be written

$$\Phi(r) = \Phi_0 \exp\left(-\frac{L}{2\xi}\right) \sinh\left(\frac{L-2r}{2\xi}\right), \quad (19)$$

where L is the effective length of the box, which is taken to be a free parameter. Some numerical data are shown in Fig. 8, together with a fit of eq. (19). The fitted values of ξ for all data sets are given in Table 2. The length L turns out to be slightly larger than the extent of the lattice, as expected. We notice that the screening length is about 30% lower in the dynamical vacuum as compared to the quenched case. This does not come unexpected. In a three-dimensional model of a monopole gas with screening [30] the abelian string tension turns out to be proportional to the product of monopole density and screening length, i.e. $\sigma_{\text{ab}} \propto \rho\xi$. Though this model is an oversimplification of the underlying dynamics, it is in qualitative agreement with our findings.

Gribov copies

We shall now try to quantify the error that is made by fixing to a local maximum of $F[U]$ instead of the global one. We follow the procedure suggested in [8]. The test runs are done on the $16^3 32$ lattice at $\beta = 5.29$, $\kappa = 0.135$ using a total of $O(50)$ configurations. We create 20 random gauge copies for each configuration, employing the SA algorithm. Then we randomly pick n gauge copies out of each set (of 20) and select the copy with the highest value of $F[U]$ to compute our observable \mathcal{O} . Obviously the result will depend on n , and the true result is obtained at $n \rightarrow \infty$. The approach to $n = \infty$ may be

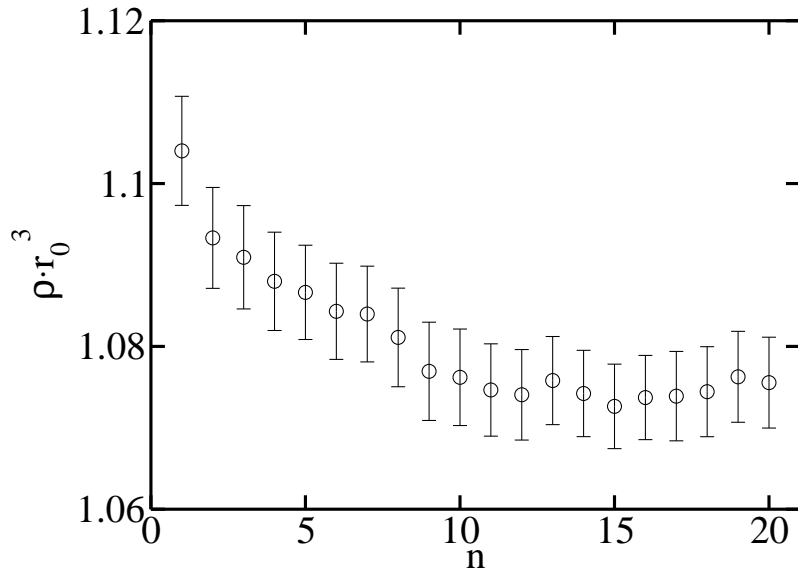


Fig. 9. The monopole density on the $16^3 32$ lattice at $\beta = 5.29$, $\kappa = 0.135$, and its dependence on the number of Gribov copies.

fitted by [37]

$$\langle \mathcal{O} \rangle(n) = \langle \mathcal{O} \rangle(\infty) + \frac{\text{const.}}{n}. \quad (20)$$

In Fig. 9 we show the monopole density as a function of n . We see that ρ reaches a plateau at $n \approx 10$. By taking only one gauge copy into account one introduces a systematic error of the order of 3%. The effect of Gribov copies is slightly stronger in case of the abelian static potential, as can be inferred from Figs. 10 and 11. Here the systematic error is about 6%, while iterative gauge fixing might lead to a discrepancy of $O(20\%)$.

4 Color electric flux tube

Studies of the pure $SU(2)$ gauge theory in the MAG [38,39,40] have shown that the expectation values of the static color electric field and the monopole currents satisfy, to a good accuracy, the classical equations of motion and dual Ampère’s law, in agreement with the dual superconductor picture of confinement.

In this section we present first results of the microscopic structure of the color electric flux tube in full QCD and in the pure $SU(3)$ gauge theory. It is expected that long-range forces between quarks remain to exist in the dynamical theory as well, because the color charge of quarks cannot be screened locally by Higgs scalars (made out of gluons).

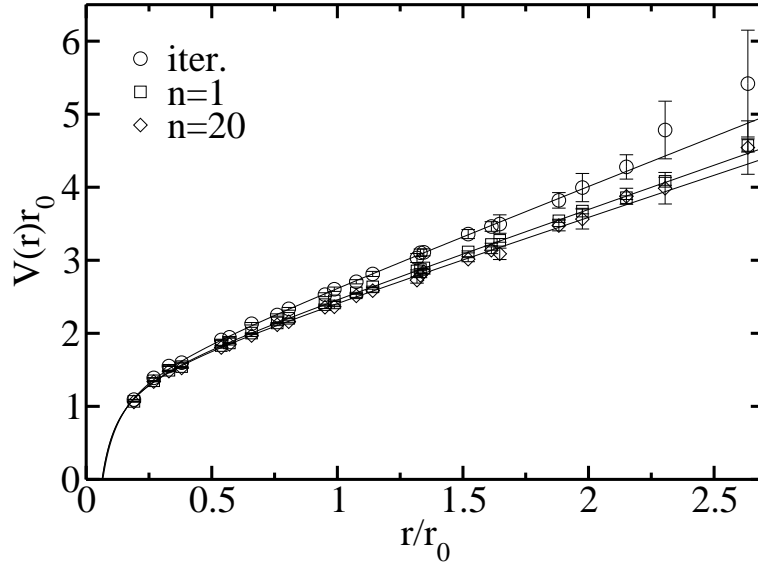


Fig. 10. The abelian static potential on the $16^3 32$ lattice at $\beta = 5.29$, $\kappa = 0.135$, and its dependence on the number of Gribov copies. Also shown is the result of the iterative gauge fixing.

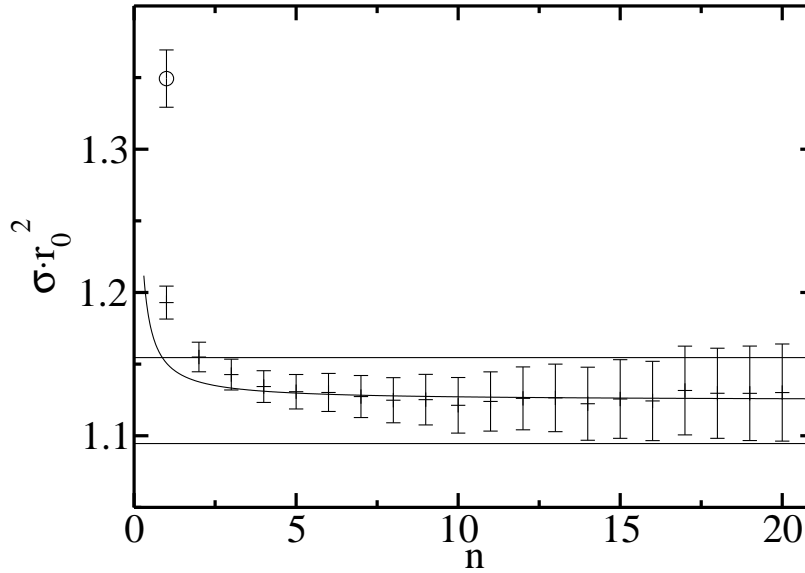


Fig. 11. The abelian string tension on the $16^3 32$ lattice at $\beta = 5.29$, $\kappa = 0.135$, and its dependence on the number of Gribov copies, together with the result of the iterative gauge fixing (\circ).

Observables

We will primarily be concerned with local abelian operators

$$\mathcal{O}(s) = \text{diag}(\mathcal{O}_1(s), \mathcal{O}_2(s), \mathcal{O}_3(s)) \in U(1) \times U(1). \quad (21)$$

For C-parity even operators, such as the action density and the monopole density, the correlator of $\mathcal{O}(s)$ with the abelian Wilson loop \mathcal{W}_C is given by [41]

$$\langle \mathcal{O}(s) \rangle_{\mathcal{W}} \equiv \frac{1}{3} \frac{\langle \text{Tr} \mathcal{O}(s) \text{Tr} \mathcal{W}_C \rangle}{\langle \text{Tr} \mathcal{W}_C \rangle} - \frac{1}{3} \langle \text{Tr} \mathcal{O} \rangle. \quad (22)$$

For C-parity odd operators \mathcal{O} , such as the color electric field and the monopole current, we have

$$\langle \mathcal{O}(s) \rangle_{\mathcal{W}} \equiv \frac{\langle \text{Tr} (\mathcal{O}(s) \mathcal{W}_C) \rangle}{\langle \text{Tr} \mathcal{W}_C \rangle}, \quad (23)$$

in analogy to the case of $SU(2)$ [38,39,42,43].

The action density $\rho_A^{\mathcal{W}}$, the color electric field $E_i^{\mathcal{W}}$, the monopole current $k^{\mathcal{W}}$ and the monopole density $\rho_M^{\mathcal{W}}$, induced by the Wilson loop, are then given by

$$\rho_A^{\mathcal{W}}(s) = \frac{\beta}{3} \sum_{\mu > \nu} \langle \text{diag}(\cos(\theta_1(s, \mu, \nu)), \cos(\theta_2(s, \mu, \nu)), \cos(\theta_3(s, \mu, \nu))) \rangle_{\mathcal{W}}, \quad (24)$$

where $\theta_i(s, \mu, \nu) \equiv \arg(u_i(s, \mu, \nu))$ is the plaquette angle,

$$E_j^{\mathcal{W}}(s) = i \langle \text{diag}(\theta_1(s, 4, j), \theta_2(s, 4, j), \theta_3(s, 4, j)) \rangle_{\mathcal{W}}, \quad (25)$$

$$k^{\mathcal{W}}(*s, \mu) = 2\pi i \langle \text{diag}(k_1(*s, \mu), k_2(*s, \mu), k_3(*s, \mu)) \rangle_{\mathcal{W}}, \quad (26)$$

and

$$\rho_M^{\mathcal{W}}(s) = \frac{1}{4} \sum_{\mu} \langle \text{diag}(|k_1(*s, \mu)|, |k_2(*s, \mu)|, |k_3(*s, \mu)|) \rangle_{\mathcal{W}}, \quad (27)$$

respectively. Out of the three ‘color’ components of the observables only two are independent. In the following we shall take the average of the three components.

As before, we take \mathcal{C} to be a loop of spatial extent R and temporal extent T . The four corners of the loop are placed at $(-R/2, 0, 0, 0)$, $(R/2, 0, 0, 0)$, $(-R/2, 0, 0, T)$ and $(R/2, 0, 0, T)$, and $s_4 = T/2$ will be taken throughout this section.

Abelian flux tube

Let us first consider the profile of the abelian flux tube. We take $R = 10$, which on our lattices corresponds to a spatial separation of the static sources of ≈ 1 fm, and $T = 6$. We checked the T dependence of part of our results

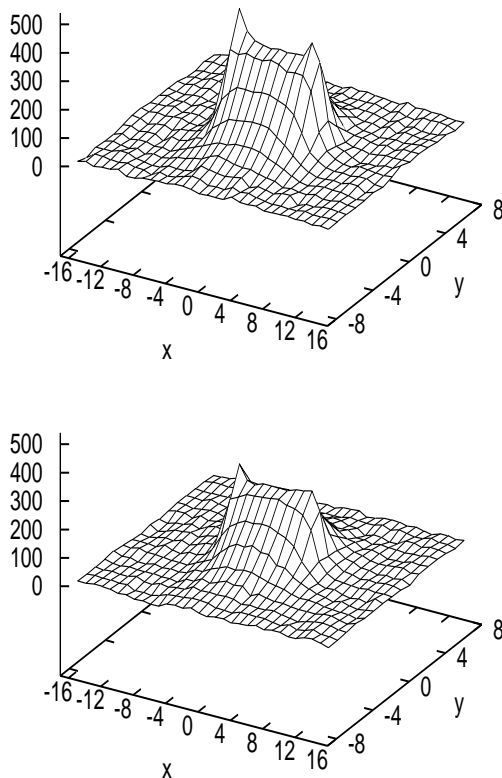


Fig. 12. The action density $\rho_A^W(s) r_0^4$ of the Abelian flux tube as a function of $x = s_1$, $y = s_2$ at $z = s_3 = 0$ on the $16^3 32$ lattice in full (top) and quenched QCD (bottom) at $\beta = 5.20$, $\kappa = 0.1355$ and $\beta = 6.0$, respectively.

by comparing the numbers to $T = 5$ and found only insignificant changes, albeit for $R = 6$, which justifies our choice. The spatial links are smeared as described in (12).

In the following we shall also use the notation $x = s_1$, $y = s_2$ and $z = s_3$. In Figs. 12 and 13 we show the action density $\rho_A^W(s)$ in full and quenched QCD, respectively. It appears that the action density in full QCD is higher than in the quenched case, while their shapes are quite similar.

We estimate the width δ of the abelian flux tube by fitting our data at $x = 0$ to the function

$$\rho_A(r_\perp) = \text{const.} \exp\left(- (r_\perp - \epsilon)^2 / \delta^2\right), \quad (28)$$

where r_\perp is the distance of s from the line connecting the static sources at $s_4 = T/2$, and ϵ is a displacement parameter of $O(a)$ accounting for a small shift of the true action density from its entry at s . We obtain $\delta = 0.29(1)$ fm, both in full and quenched QCD. This is a surprisingly small number, much smaller than any hadron radius. It tells us, in particular, that already at interquark distances $\gtrsim 0.5$ fm the string model of hadrons becomes effective.

In Figs. 14 and 15 we show the distribution of the color electric field $E_1^{\mathcal{W}}$ in and around the flux tube. The electric field is purely longitudinal in a narrow region between the sources of diameter \approx six lattice spacings and practically zero outside. We fit $E_1^{\mathcal{W}}$ at $x, z = 0$ and for $y/r_0 > 0.5$ to an exponential:

$$E_1^{\mathcal{W}} = \text{const.} \exp(-y/\lambda). \quad (29)$$

For the penetration length we find $\lambda = 0.15(1)$ fm in full QCD and $\lambda = 0.17(1)$ fm in the quenched case. Whether the flux tube indeed narrows down in full QCD needs to be confirmed with higher statistics.

In Figs. 16 we show the monopole density $\rho_M^{\mathcal{W}}(s)$. We see again that outside the flux tube the monopole density is more than two times larger in full QCD than in the quenched case. Inside the flux tube the monopole density is strongly suppressed. This indicates that the expectation value of the dual Higgs field vanishes inside the flux tube, in agreement with the dual superconductor model of the vacuum. In this model we furthermore expect that the monopole currents forms a solenoidal (i.e. azimuthal) supercurrent which constricts the color electric field into flux tubes, thereby satisfying the dual Ampère law:

$$\vec{k} = \vec{\nabla} \times \vec{E}^{\mathcal{W}}. \quad (30)$$

In Fig. 17 we show the transverse components of the monopole current at $x = 0$ in the (y, z) plane (i.e. perpendicular to the flux tube), and in Fig. 18 we compare the l.h.s and r.h.s. of eq. (30). In the latter figure $R = 6$ was used in order to reduce the errors. We find that the dual Ampère law is approximately satisfied in both full and quenched QCD. So far this has only been verified in the pure $SU(2)$ gauge theory [38,39].

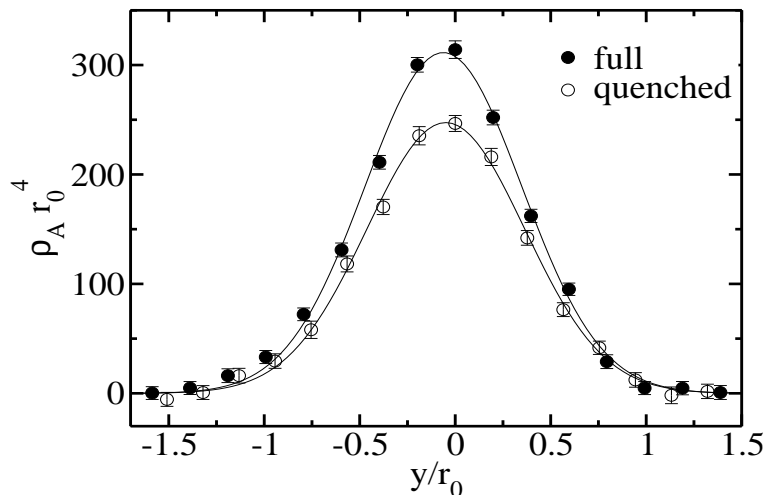


Fig. 13. The action density $\rho_A^{\mathcal{W}}(s) r_0^4$ of Fig. 12 plotted across the flux tube at $x = 0$.

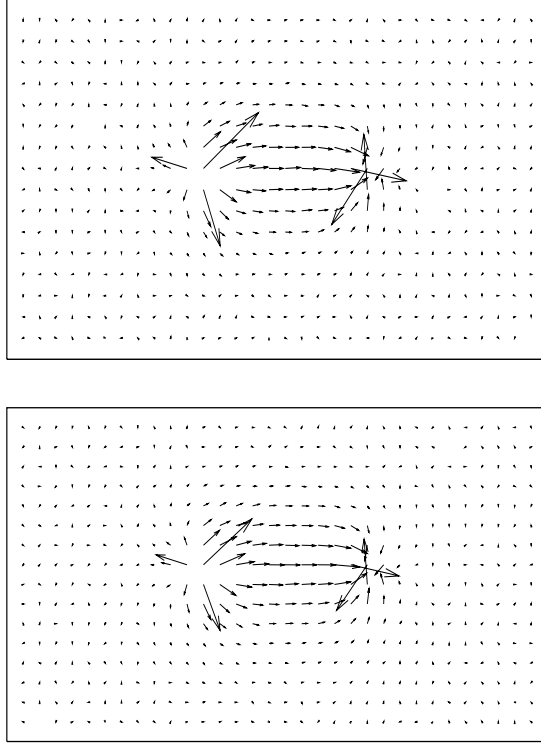


Fig. 14. Distribution of the color electric field $\vec{E}^{\mathcal{W}}$ in full (top) and quenched QCD (bottom) in the (x,y) plane for the same lattices as in Fig. 12. The magnitude of $E^{\mathcal{W}}$ is indicated by the length of the arrows.

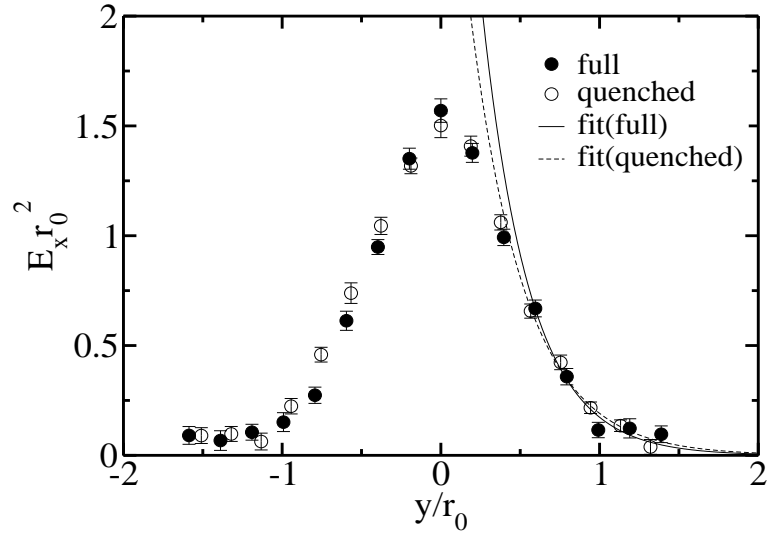


Fig. 15. The color electric field $E_1^{\mathcal{W}}$ of Fig. 14 plotted across the flux tube at $x = 0$.

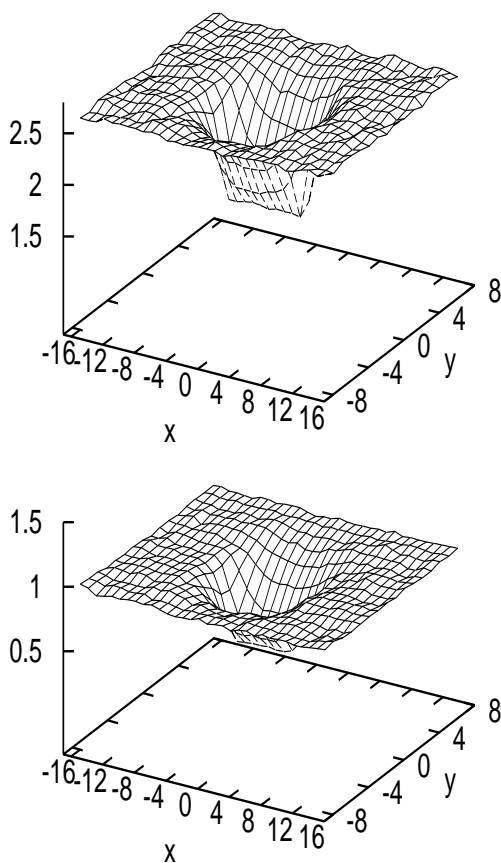


Fig. 16. The monopole density $\rho_M^{\mathcal{W}}(s)r_0^3$ as a function of x, y at $z = 0$ in full (top) and quenched QCD (bottom) for the same lattices as in Fig. 12.

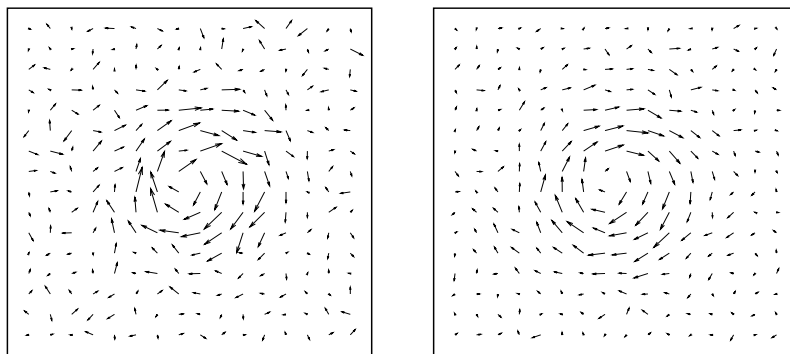


Fig. 17. The solenoidal monopole current $k^{\mathcal{W}}r_0^3$ in the (y, z) plane (i.e. perpendicular to the flux tube) at $x = 0$ in full (left) and quenched QCD (right) for the same lattices as in Fig. 12.

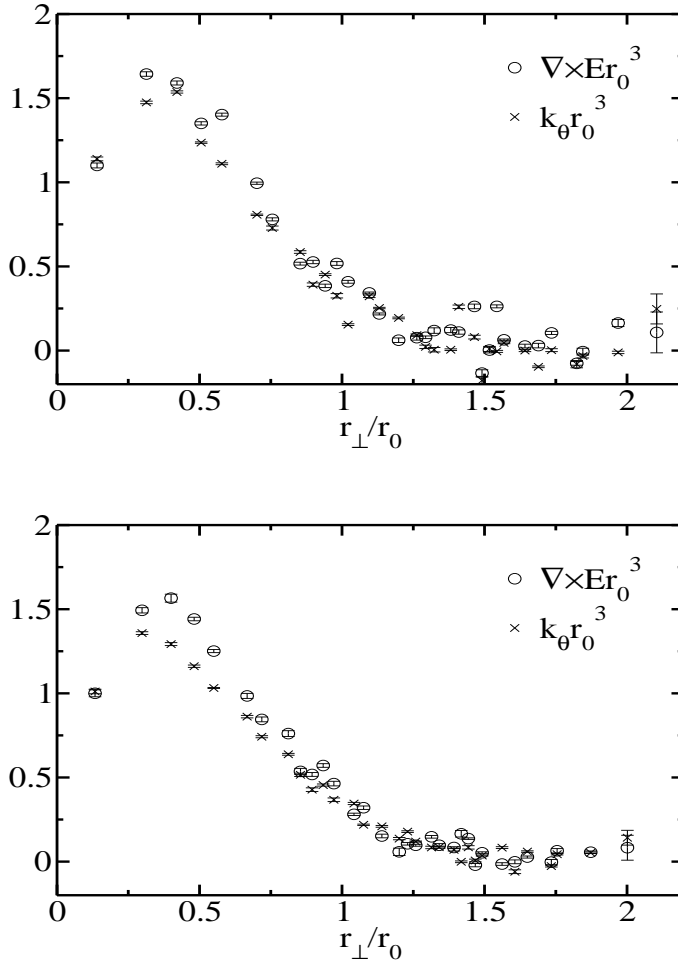


Fig. 18. Test of dual Ampère's law in full (top) and quenched QCD (bottom) for the same lattices as in Fig. 12.

Monopoles versus photons

Further insight into the confinement mechanism can be obtained by probing the flux tube in terms of the monopole and photon part of the abelian gauge field separately. To do so, we simply have to replace the lattice abelian gauge field $\theta_i(s, \mu)$ in the various probes by $\theta_i^{\text{mon}}(s, \mu)$ and $\theta_i^{\text{ph}}(s, \mu)$, respectively. We have done calculations in full QCD (here on the $24^3 48$ lattice at $\beta = 5.29$, $\kappa = 0.1355$) and in the quenched theory. To enhance the signal, the monopole and photon fields are smeared as before. Qualitatively, we find no difference between full QCD and the quenched theory.

In Fig. 19 we show the action density $\rho_A^{\mathcal{W}}$ of the monopole and photon part of the gauge field. We see that the action density originates almost entirely

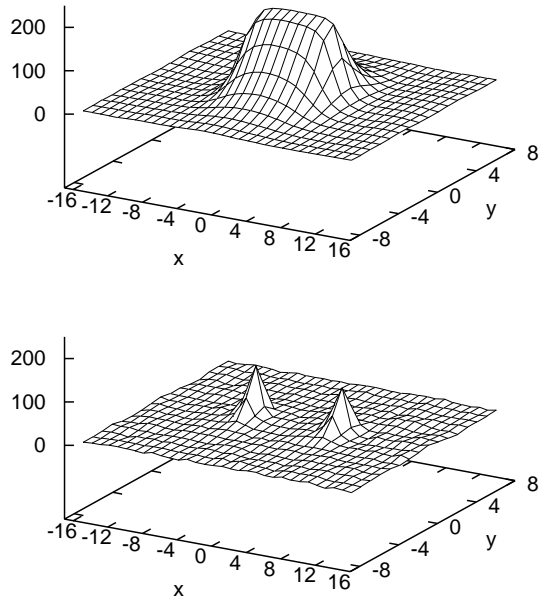


Fig. 19. Monopole (top) and photon part (bottom) of the action density $\rho_A^{\mathcal{W}} r_0^4$ on the (quenched) $16^3 32$ lattice at $\beta = 6.0$.

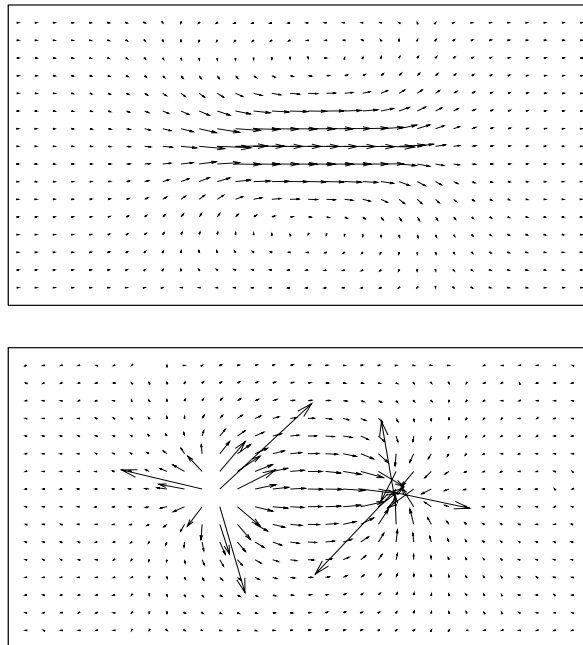


Fig. 20. Distribution of the monopole (top) and photon part of the color electric field $\vec{E}^{\mathcal{W}}$ (bottom) on the $16^3 32$ lattice at $\beta = 6.0$. For better visibility the monopole part is enhanced by a factor of two relative to the photon part.

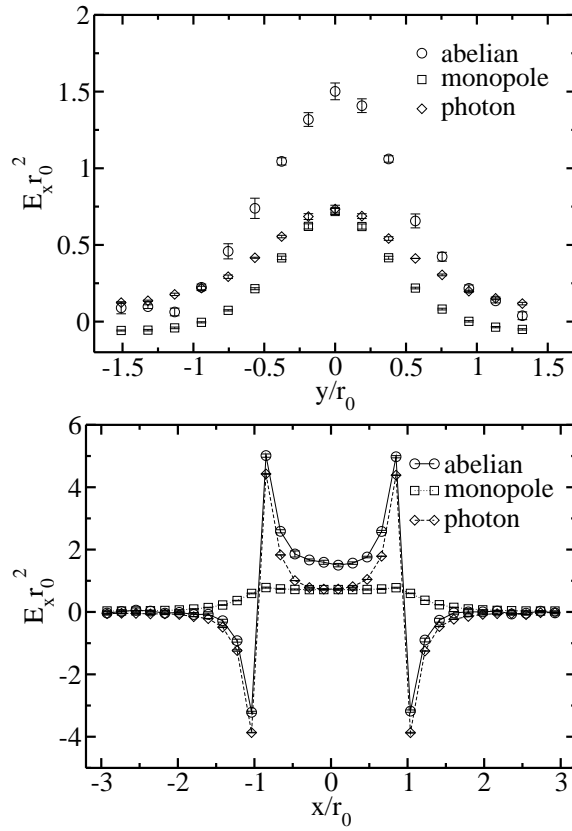


Fig. 21. Monopole and photon part of the color electric field E_1^V in the (y,z) plane at $x = 0$ (top) and parallel to the flux tube (bottom).

from the monopole part, while the photon contributes a Coulomb field around the static charges only. The width of the flux tube is unchanged: $\delta = 0.29(1)$ fm as before. In Figs. 20 and 21 we show the distribution of the color electric field. We see that the monopole part of the field has no sources. The sources show up in the photon part only. We furthermore see that outside the flux tube the monopole and photon parts of the electric field largely cancel, while they add in the interior of the tube. We have attempted to fit the photon field by a Coulomb ansatz. While the transverse component could be well fitted, we failed for the longitudinal component (i.e. parallel to the flux tube).

String breaking

In the presence of dynamical quarks we expect that the flux tube (string) breaks if the static charges are separated far enough. It has been estimated that this will happen at a distance of ≈ 1.2 fm for our quark masses of $m_q \approx 100$ Mev [14,44]. This does not mean that the string state vanishes from the spectrum of the transfer matrix. It only ceases to be the state of lowest energy in the corresponding channel. In QCD string breaking has so far only been

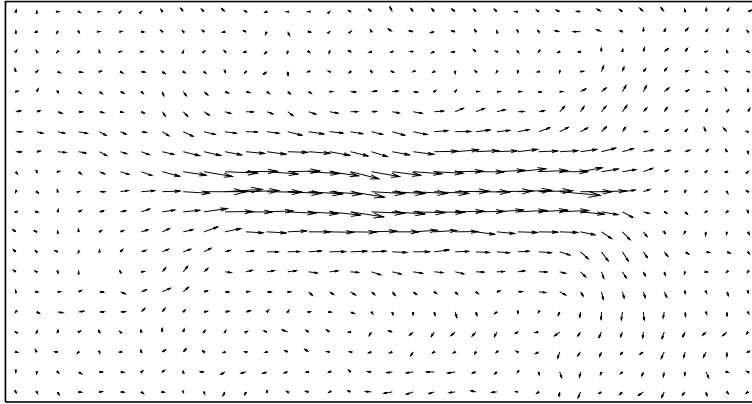


Fig. 22. The monopole part of the color electric field \vec{E}^W on the $24^3 48$ lattice. Only the region $-18 \leq x \leq 17$, $-10 \leq y \leq 9$ is shown.

observed at finite temperature close to the deconfining phase transition [45], but never at zero temperature [14,15,16,46]. The recent finding [47] of string breaking from Wilson loops in the case of adjoint quarks in three-dimensional $SU(2)$ gauge theory indicates that that this should be possible at zero temperature too. Though our prime motivation for the following investigation was to detect string breaking and shed some light on the dynamics that drives it, we like to stress that the unbroken string is of quite some interest as well from the point of view of the confinement problem.

The calculations in this section are done on the $24^3 48$ lattice at $\beta = 5.29$, $\kappa = 0.1355$. On this lattice $m_\pi/m_\rho \approx 0.7$. The difference to our previous calculation is that we consider large Wilson loops. We take $R = 18$, which corresponds to a separation of the static charges of ≈ 1.6 fm, and $T = 10$. It is important to choose T large as well in order to increase the chance of string breaking [48]. In Fig. 22 we show the monopole part of the color electric field \vec{E}^W . The restriction to the monopole part allowed us to obtain a clean signal even at $x = 0$. We do not observe any sign of string breaking. Furthermore, the flux tube does not show any broadening effect. A fit of the form (28) gives $\delta = 0.30(3)$ fm at $x = 0$. The same value was found for $R = 10$. If the long-range properties of QCD were described by the Nambu-Goto effective string action, we would have expected the transverse extension of the flux tube to increase logarithmically with R [49]. A similar observation has been made in the pure $SU(2)$ gauge theory [50]. Perhaps the abelian flux tube is described by the Ramond effective string action instead, which does not give rise to any broadening effect [51].

It is perhaps not surprising that we do not observe any string breaking (yet) [52]. String breaking is expected to occur if $\exp(-2E_{sl}(R + T)) > \exp(-\sigma RT)$, where E_{sl} is the binding energy of the static-light meson. This is only the case if $T \gtrsim 3$ fm [16].

5 Effective monopole action

We have seen that the vacuum undergoes several changes if dynamical color electric charges are introduced. We shall study now how this will affect the effective monopole action.

There are three types of monopole currents (8), of which two are independent. For simplicity we take into account only one of them, thus integrating out the other two [53]. For the time being, we assume the form of the effective monopole action in full QCD to be the same as in the quenched theory [54]. It is composed of 27 types of two-point interactions, one four-point interaction and one six-point interaction:

$$S(k) = \sum_{i=1}^{29} G_i S_i(k), \quad (31)$$

where G_i are the coupling constants which need to be determined. This we will do by employing an extended Swendsen method [20]. In this section we shall write $k(s, \mu)$ instead of $k(*s, \mu)$ for the sake of simplicity. Explicitly, we then have:

Two-point interaction for parallel currents

$$S_i(k) = \sum_s \sum_{\mu=1}^4 k(s, \mu) k_i(s, \mu), \quad i = 1, \dots, 25, \quad (32)$$

where the $k_i(s, \mu)$ are given in Table 3.

Two-point interaction for orthogonal currents

$$S_{26}(k) = \sum_s \sum_{\mu \neq \nu} k(s, \mu) k(s - \hat{\mu} - 2\hat{\nu}, \nu), \quad (33)$$

$$S_{27}(k) = \sum_s \sum_{\mu \neq \nu \neq \sigma} k(s, \mu) k(s - \hat{\mu} - 2\hat{\nu} - 2\hat{\sigma}, \sigma). \quad (34)$$

Four-point interaction

$$S_{28}(k) = \sum_s \left(\sum_{\mu=-4}^4 k(s, \mu)^2 \right)^2. \quad (35)$$

Six-point interaction

$$S_{29}(k) = \sum_s \left(\sum_{\mu=-4}^4 k(s, \mu)^2 \right)^3. \quad (36)$$

The calculations are done on the $24^3 48$ lattices listed in Table 1, both in full and quenched QCD. After fixing the gauge fields to the MAG, we employ

i	$k_i(s, \mu)$	i	$k_i(s, \mu)$
1	$k(s, \mu)$	14	$k(s + 2\hat{\mu} + \hat{\nu} + \hat{\rho}, \mu)$
2	$k(s + \hat{\mu}, \mu)$	15	$k(s + \hat{\mu} + 2\hat{\nu} + \hat{\rho}, \mu)$
3	$k(s + \hat{\nu}, \mu)$	16	$k(s + 2\hat{\nu} + \hat{\rho} + \hat{\sigma}, \mu)$
4	$k(s + \hat{\mu} + \hat{\nu}, \mu)$	17	$k(s + 2\hat{\mu} + \hat{\nu} + \hat{\rho} + \hat{\sigma}, \mu)$
5	$k(s + \hat{\nu} + \hat{\rho}, \mu)$	18	$k(s + \hat{\mu} + 2\hat{\nu} + \hat{\rho} + \hat{\sigma}, \mu)$
6	$k(s + 2\hat{\mu}, \mu)$	19	$k(s + 2\hat{\mu} + 2\hat{\nu}, \mu)$
7	$k(s + 2\hat{\nu}, \mu)$	20	$k(s + 2\hat{\nu} + 2\hat{\rho}, \mu)$
8	$k(s + \hat{\mu} + \hat{\nu} + \hat{\rho} + \hat{\sigma}, \mu)$	21	$k(s + 3\hat{\mu}, \mu)$
9	$k(s + \hat{\mu} + \hat{\nu} + \hat{\rho}, \mu)$	22	$k(s + 3\hat{\nu}, \mu)$
10	$k(s + \hat{\nu} + \hat{\rho} + \hat{\sigma}, \mu)$	23	$k(s + 2\hat{\mu} + 2\hat{\nu} + \hat{\rho}, \mu)$
11	$k(s + 2\hat{\mu} + \hat{\nu}, \mu)$	24	$k(s + \hat{\mu} + 2\hat{\nu} + 2\hat{\rho}, \mu)$
12	$k(s + \hat{\mu} + 2\hat{\nu}, \mu)$	25	$k(s + 2\hat{\nu} + 2\hat{\rho} + \hat{\sigma}, \mu)$
13	$k(s + 2\hat{\nu} + \hat{\rho}, \mu)$		

Table 3

The monopole currents $k_i(s, \mu)$ entering eq. (32).

a type-II block spin transformation [55] with up to $n = 4$ blocking steps. The final outcome is an action at the physical length scale $b = na$. We believe that the monopole action is effective at scales $0.4 \lesssim b \lesssim 0.8$ fm.

In Fig. 23 we show the self-coupling G_1 as a function of b . We see that in full QCD G_1 is systematically smaller than in the quenched theory for all values of b . In Fig. 24 we plot the self-coupling G_1 as a function of m_π/m_ρ for our smallest b value. We find that G_1 decreases with decreasing quark mass.

A necessary condition for monopole condensation is $G_1 \leq \ln 7$. This is achieved for $b \gtrsim 0.27$ fm in full QCD and for $b \gtrsim 0.35$ fm in the quenched theory. In Fig. 25 we show the coupling constants G_2 and G_3 . We see that in full QCD G_2 is systematically smaller than in the quenched theory for all values of b , as in the case of G_1 , while G_3 shows the opposite behavior. The other coupling constants show little difference between full and quenched QCD. In Fig. 26 we show, as an example, G_{28} and G_{29} . Because the magnetic charge of the monopoles is in almost all cases ± 1 , and G_1 is the dominant coupling constant, the monopole action can be approximated by $G_1 L$, where L is the length of the monopole loop. As a result, a smaller self-coupling G_1 will give rise to a larger value of L and a larger monopole density, and vice versa. This is to say that both observations, namely that the monopole density increases and the self-coupling decreases with decreasing quark mass, are consistent with each other.

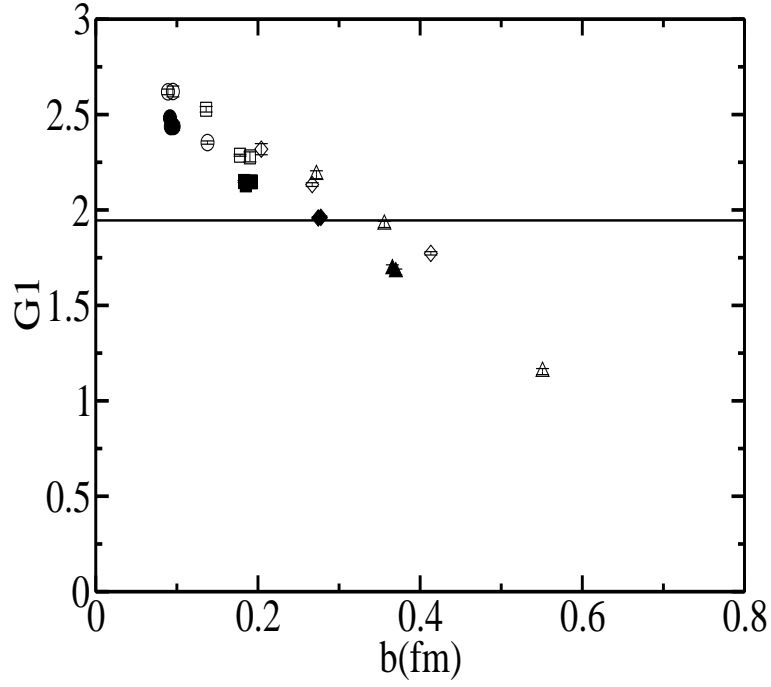


Fig. 23. The monopole self-coupling G_1 , as a function of the physical length scale b . The symbols are: $n = 1$ (\bullet), $n = 2$ (\blacksquare), $n = 3$ (\blacklozenge), $n = 4$ (\blacktriangle) in full QCD, and $n = 1$ (\circ), $n = 2$ (\square), $n = 3$ (\diamond), $n = 4$ (\triangle) in quenched QCD.

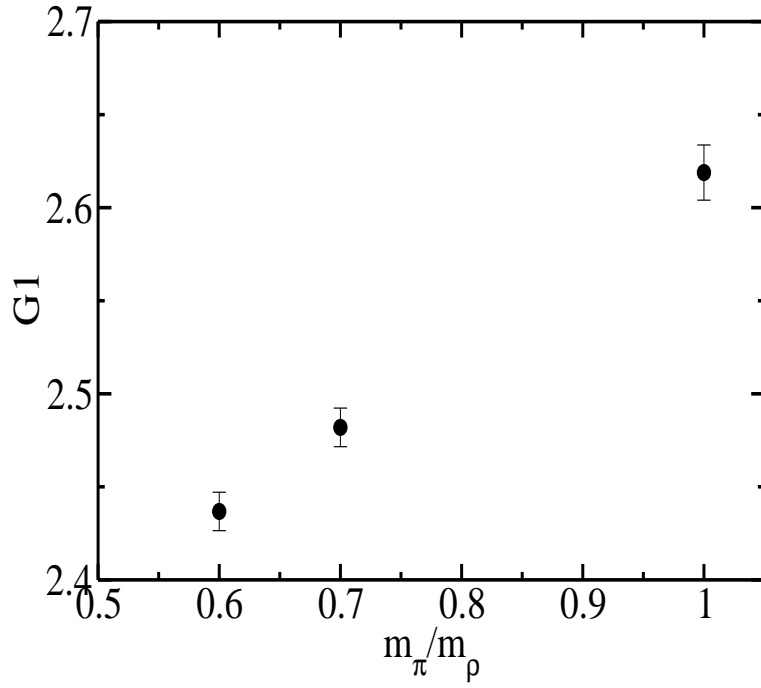


Fig. 24. The dependence of G_1 on the ratio m_π/m_ρ for $b = 0.09$ fm. The entry at $m_\pi/m_\rho = 1$ corresponds to the quenched theory.

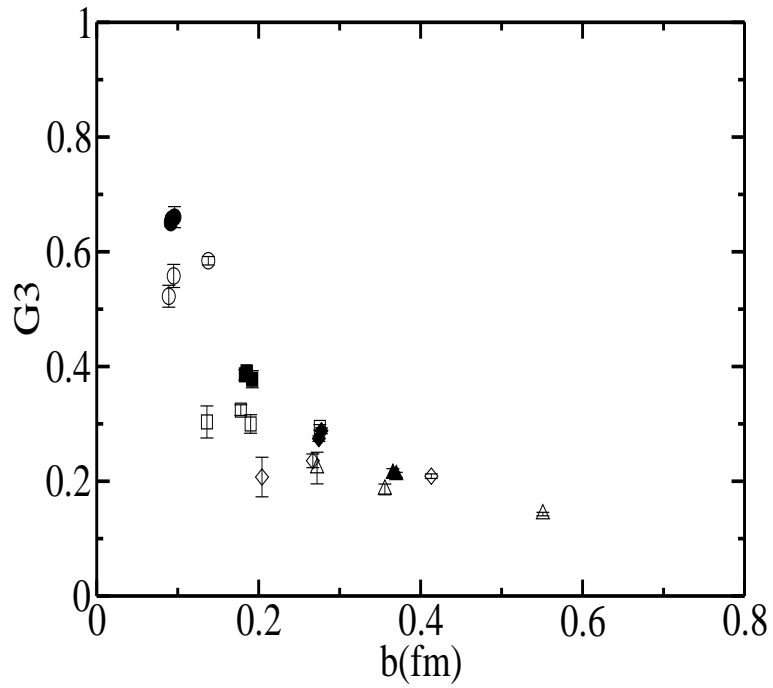
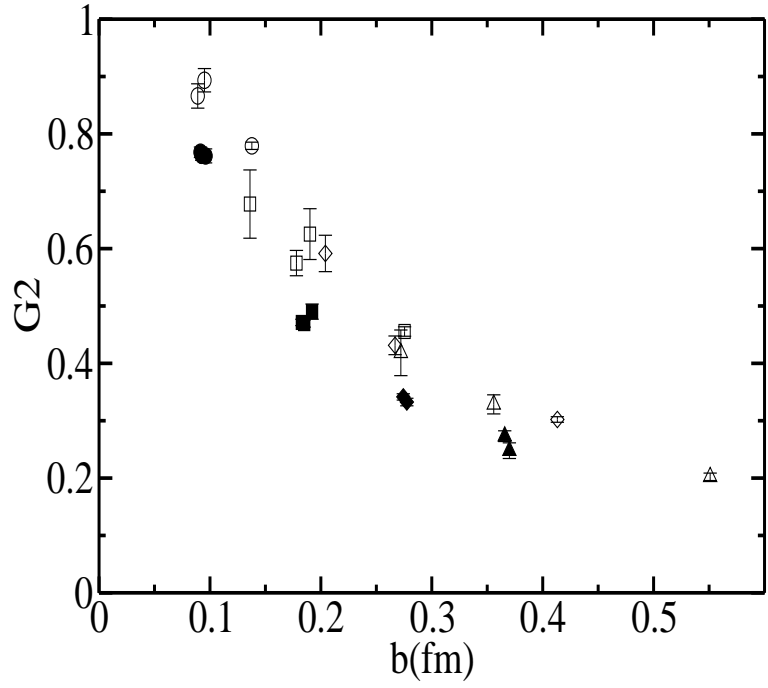


Fig. 25. The coupling constants G_2 and G_3 as a function of b . The symbols are as in Fig. 23.

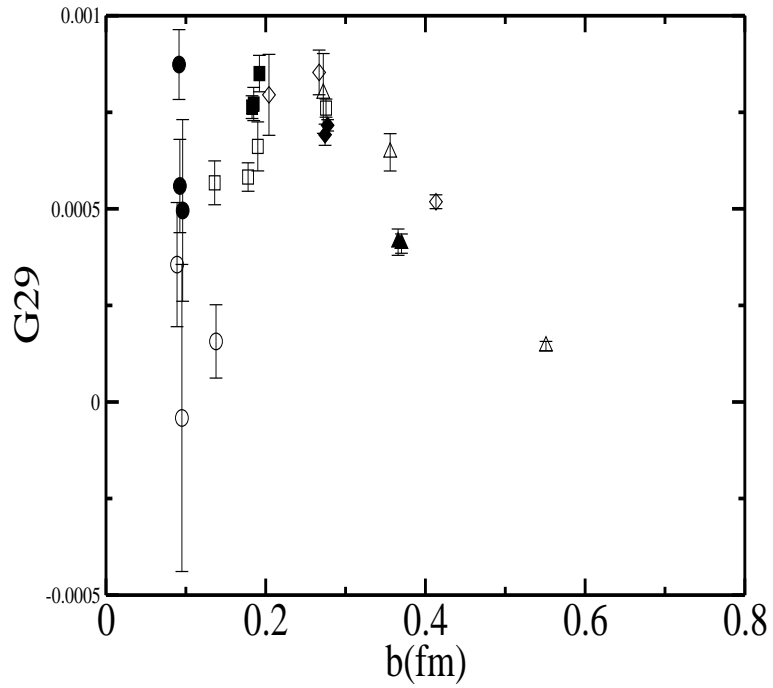
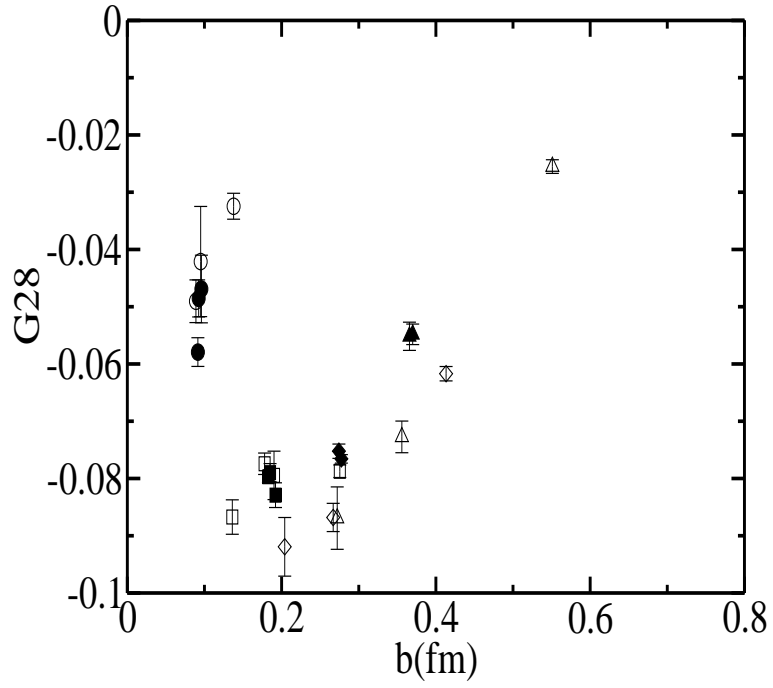


Fig. 26. The coupling constants G_{28} and G_{29} of the four-point and six-point interactions, respectively, as a function of b . The symbols are as in Fig. 23.

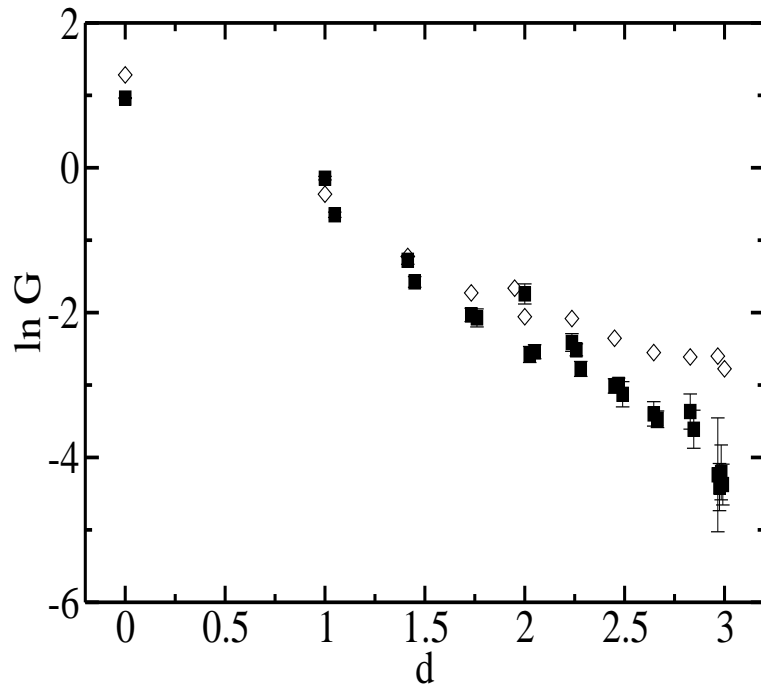
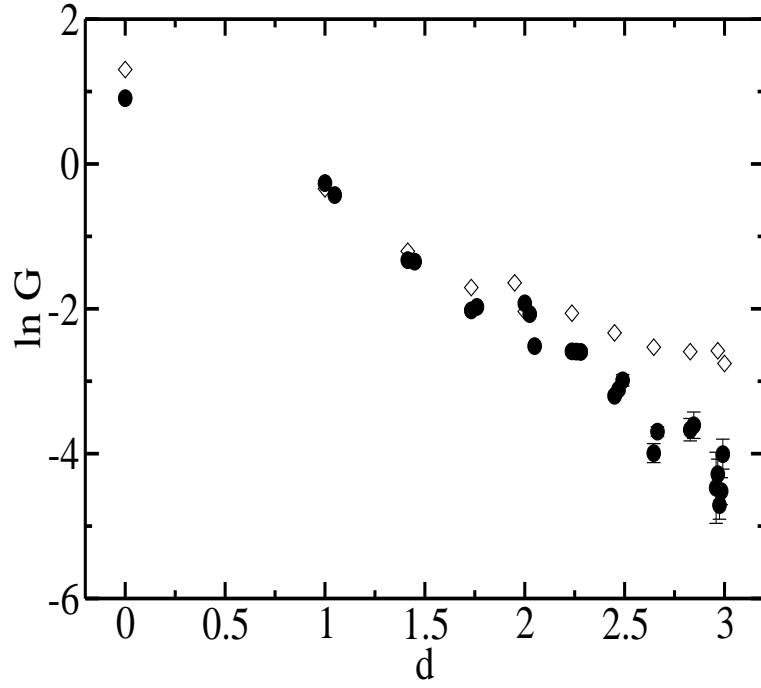


Fig. 27. The two-point coupling G of the monopole currents $k(s, \mu)$ and $k(s', \mu)$ as a function of distance $d = \sqrt{\sum_{\mu} (s_{\mu} - s'_{\mu})^2}$ in full (●) and quenched QCD (■), compared to the Coulomb propagator (◇).

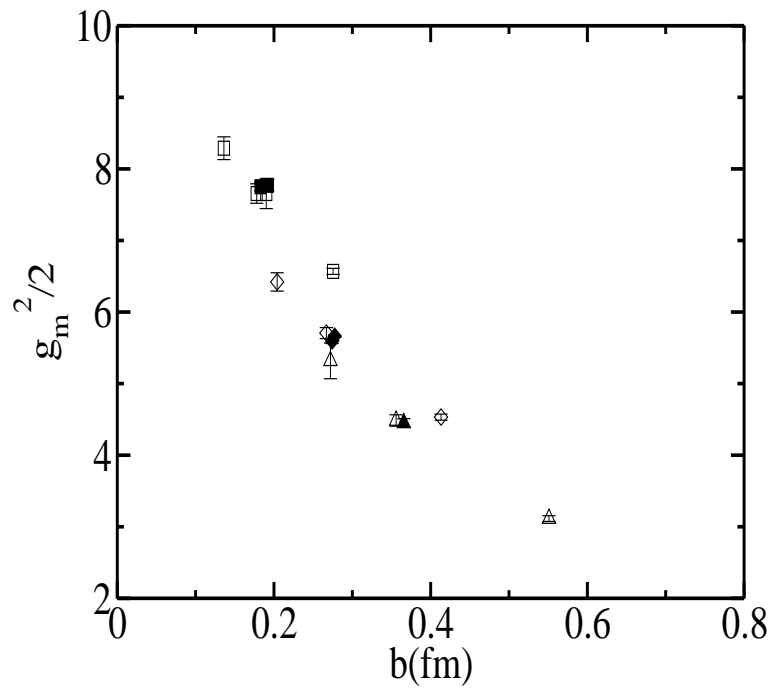
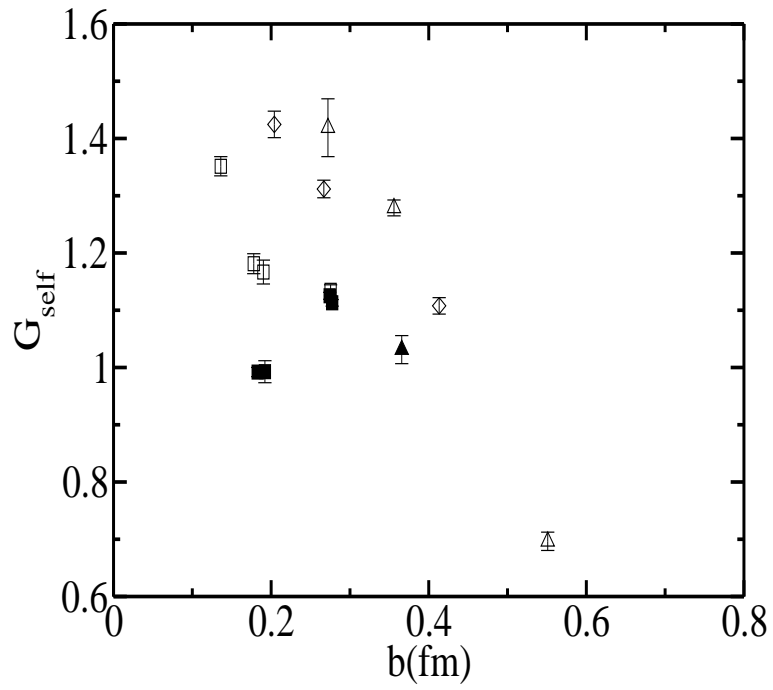


Fig. 28. The self-coupling G_{self} and the Coulomb coupling g_m as a function of b . The symbols are as in Fig. 23.

To shed further light on the dynamics of the monopoles we have looked at the coupling G of two ($n = 1$) parallel monopole currents, $k(s, \mu)$ and $k(s', \mu)$, as a function of the distance $d = \sqrt{\sum_{\mu} (s_{\mu} - s'_{\mu})^2}$ between them. In Fig. 27 we show G together with the lattice Coulomb propagator. We see that at distances $d \gtrsim 2$ the interaction becomes weaker than Coulomb in both full and quenched QCD. This is consistent with the screening effect discussed in Section 3. We do not see any difference between full QCD and quenched QCD though.

We may parameterize the effective monopole action by

$$S(k) = S_{\text{Coulomb}} + S_{\text{self}} + S_{4\text{-point}} + S_{6\text{-point}} + S_{\text{add}}, \quad (37)$$

where

$$S_{\text{Coulomb}} = \frac{g_m^2}{2} \sum_{s,s'} \sum_{\mu=1}^4 k(s, \mu) \Delta^{-1}(s - s') k(s', \mu),$$

$$S_{\text{self}} = G_{\text{self}} S_1(k),$$

$$S_{4\text{-point}} = G_{4\text{-point}} S_{28}(k), \quad (38)$$

$$S_{6\text{-point}} = G_{6\text{-point}} S_{29}(k),$$

and S_{add} includes 12 additional two-point interaction terms. In Fig. 28 we show the self-coupling G_{self} and the Coulomb coupling g_m . It is interesting to see that in full QCD G_{self} is smaller than in the quenched case, while the Coulomb coupling is almost unchanged. Corrections to the Coulomb interaction are found to be very small in the infrared region.

6 Conclusions

We have performed a detailed study of the dynamics of the QCD vacuum, thereby focussing on the abelian degrees of freedom in the MAG. Our main objective was to find out how the vacuum reacts to the introduction of dynamical color electric charges (quarks). The monopole density was found to increase by more than a factor of two if we decrease the quark mass from $m_{\pi}/m_{\rho} = 1$ (the quenched limit) to $m_{\pi}/m_{\rho} \approx 0.6$, both for the total number of monopoles and for the monopoles in the infrared clusters. Related to that, we found that the magnetic screening length decreased by 30% over that range. The string tension, the static potential and the structure of the flux tube, on the other hand, remained almost the same. We verified the dual Ampère law in full QCD and in the pure $SU(3)$ gauge theory. This result lends further support to the dual superconductor model of the vacuum in full and quenched QCD. The width of the abelian flux tube was found to be $\delta = 0.29(1)$ fm in both cases. Another characteristic feature of the flux tube is the penetration length. We obtained $\lambda = 0.15(1)$ fm in full QCD and $\lambda = 0.17(1)$ fm in the

quenched case. This results in a dual photon mass of 1.3(1) GeV and 1.2(1) GeV, respectively. Decomposing the abelian gauge field into monopole and photon parts allowed us to study flux tubes up to a length of ≈ 1.6 fm in full QCD. No signal of string breaking was found. Comparing flux tubes of various lengths R , it turned out that the width of the flux tube does not depend on R , contrary to the prediction of the Nambu-Goto effective string theory. The effective monopole action was determined. In full QCD the monopole self-coupling was found to be systematically smaller than in the quenched theory. The main contributions to the effective monopole action are found to be the self-interaction and the Coulomb interaction.

Acknowledgements

We wish to thank the UKQCD collaboration for letting us use their dynamical gauge field configurations at $\beta = 5.2$, and A. Irving for computing r_0/a on all configurations. Furthermore, we would like to thank G. Bali, A. Hart, T. Kovacs, M. Müller-Preussker and H. Suganuma for useful discussions. H.I. thanks the Humboldt University and the Kanazawa University for hospitality. V.G.B. acknowledges support from JSPS RC 30126103. The numerical calculations have been done on the COMPAQ Alpha Server ES40 at Humboldt University and on the SX5 at RCNP, Osaka University. T.S. is supported by JSPS Grant-in-Aid for Scientific Research on Priority Areas 13135210 and (B) 15340073. M.I.P. is partially supported by grants RFBR 02-02-17308, RFBR 01-02-17456, INTAS-00-00111, DFG-RFBR 436 RUS 113/739/0, RFBR-DFG 03-02-04016, and CRDF award RPI-2364-MO-02.

References

- [1] G. 't Hooft, Nucl. Phys. **B190** (1981) 455.
- [2] A.S. Kronfeld, M.L. Laursen, G. Schierholz and U.-J. Wiese, Phys. Lett. **B198** (1987) 516.
- [3] A.S. Kronfeld, G. Schierholz and U.-J. Wiese, Nucl. Phys. **B293** (1987) 461.
- [4] K. Amemiya and H. Suganuma, Phys. Rev. **D60** (1999).
- [5] V.G. Bornyakov, M.N. Chernodub, F.V. Gubarev, S.M. Morozov and M.I. Polikarpov, Phys. Lett. **B559** (2003) 214.
- [6] H. Shiba and T. Suzuki, Phys. Lett. **B351** (1995) 519.
- [7] H. Shiba and T. Suzuki, Phys. Lett. **B333** (1994) 461; J. Stack, S. Neiman and R. Wensley, Phys. Rev. **D50** (1994) 3399.
- [8] G.S. Bali, V. Bornyakov, M. Müller-Preussker and K. Schilling, Phys. Rev. **D54** (1996) 2863.

- [9] T. Suzuki, in *Confinement 2000*, p. 120, eds. H. Suganuma, M. Fukushima and H. Toki (World Scientific, Singapore, 2001).
- [10] A. Hart and M. Teper, Phys. Lett. **B371** (1996) 261.
- [11] V. Bornyakov and G. Schierholz, Phys. Lett. **B384** (1996) 190.
- [12] B.L.G. Bakker, M.N. Chernodub and M.I. Polikarpov, Phys. Rev. Lett. **80** (1998) 30.
- [13] O. Miyamura, Phys. Lett. **B353** (1995) 91.
- [14] C.R. Allton, S.P. Booth, K.C. Bowler, M. Foster, J. Garden, A.C. Irving, R.D. Kenway, C. Michael, J. Peisa, S.M. Pickles, J.C. Sexton, Z. Sroczynski, M. Talevi and H. Wittig, Phys. Rev. **D60** (1999) 034507.
- [15] T. Struckmann, K. Schilling, G. Bali, N. Eicker, S. Güsken, T. Lippert, H. Neff, B. Orth, W. Schroers, J. Viehoff and P. Ueberholz, Phys. Rev. **D63** (2001) 074504.
- [16] S. Aoki, G. Boyd, R. Burkhalter, S. Ejiri, M. Fukugita, S. Hashimoto, Y. Iwasaki, K. Kanaya, T. Kaneko, Y. Kuramashi, K. Nagai, M. Okawa, H.P. Shanahan, A. Ukawa and T. Yoshie, Nucl. Phys. **B** (Proc. Suppl.) **73** (1999) 216.
- [17] F. Karsch, E. Laermann and A. Peikert, Nucl. Phys. **B605** (2001) 579.
- [18] A. Ukawa, Nucl. Phys. **B** (Proc. Suppl.) **53** (1997) 106, and references therein.
- [19] Y. Mori, V. Bornyakov, M. Chernodub, Y. Koma, Y. Nakamura, T. Suzuki, M. Polikarpov, D. Sigaev, P. Uvarov, A. Veselov, A. Slavnov, G. Schierholz and H. Stüben, hep-lat/0301003.
- [20] H. Shiba and T. Suzuki, Phys. Lett. **B343**, 315 (1995); *ibid.* **B351**, 519 (1995).
- [21] V. Bornyakov, H. Ichie, S. Kitahara, Y. Koma, Y. Mori, Y. Nakamura, M. Polikarpov, G. Schierholz, T. Streuer, H. Stüben and T. Suzuki, Nucl. Phys. **B** (Proc. Suppl.) **106** (2002) 634.
- [22] S. Booth, M. Göckeler, R. Horsley, A.C. Irving, B. Joo, S. Pickles, D. Pleiter, P.E.L. Rakow, G. Schierholz, Z. Sroczynski and H. Stüben, Phys. Lett. **B519** (2001) 229, and to be published. The r_0/a values given have been updated by A. Irving, privat communication.
- [23] K. Jansen and R. Sommer, Nucl. Phys. **B530** (1998) 185.
- [24] S. Necco and R. Sommer, Nucl. Phys. **B622** (2002) 328.
- [25] F. Brandstaeter, U.-J. Wiese and G. Schierholz, Phys. Lett. **B272** (1991) 319.
- [26] G.S. Bali, V. Bornyakov, M. Müller-Preussker and F. Pahl, Nucl. Phys. **B** (Proc. Suppl.) **42** (1995) 852.

- [27] V.G. Bornyakov, E.-M. Ilgenfritz, M.L. Laursen, V.K. Mitrjushkin, M. Müller-Preussker, A.J. van der Sijs and A.M. Zadorozhnyi, Phys. Lett. **B261** (1991) 116; S. Hioki, S. Kitahara, Y. Matsubara, O. Miyamura, S. Ohno and T. Suzuki, Phys. Lett. **B271** (1991) 201.
- [28] M.I. Polikarpov and K. Yee, Phys. Lett. **B316** (1993) 333.
- [29] S. Kitahara, Y. Matsubara and T. Suzuki, Prog. Theor. Phys. **93** (1995) 1.
- [30] A. Hart and M. Teper, Phys. Rev. **D58** (1998) 014504; *ibid.* **D60** (1999) 114506.
- [31] V. Bornyakov and M. Müller-Preussker, Nucl. Phys. **B** (Proc. Suppl.) **106** (2002) 646.
- [32] A. Hasenfratz, Phys. Lett. **B476** (2000) 188.
- [33] C.R. Allton, S.P. Booth, K.C. Bowler, J. Garden, A. Hart, D. Hepburn, A.C. Irving, B. Joo, R.D. Kenway, C.M. Maynard, C. McNeile, C. Michael, S.M. Pickles, J.C. Sexton, K.J. Sharkey, Z. Sroczynski, M. Talevi, M. Teper and H. Wittig, Phys. Rev. **D65** (2002) 054502.
- [34] M. Göckeler, R. Horsley, H. Perlt, P. Rakow, G. Schierholz, A. Schiller and P. Stephenson, Phys. Rev. **D57** (1998) 5562.
- [35] J. Smit and A. van der Sijs, Nucl. Phys. **B355** (1991) 603.
- [36] T. Suzuki, S. Ilyar, Y. Matsubara, T. Okude and K. Yotsuji, Phys. Lett. **B347** (1995) 375; Erratum: *ibid.* **B351** (1995) 603.
- [37] V.G. Bornyakov, D.A. Komarov and M.I. Polikarpov, Phys. Lett. **497** (2001) 151.
- [38] R.W. Haymaker, V. Singh, Y.-C. Peng and J. Wosiek, Phys. Rev. **D53** (1996) 389.
- [39] G.S. Bali, Ch. Schlichter and K. Schilling, Phys. Rev. **D51** (1995) 5165; Prog. Theor. Phys. Suppl. **122** (1996) 67.
- [40] Y. Koma, M. Koma, T. Suzuki, E.-M. Ilgenfritz and M.I. Polikarpov, hep-lat/0210014; Y. Koma, M. Koma, E.-M. Ilgenfritz, T. Suzuki and M.I. Polikarpov, hep-lat/0302006.
- [41] G.S. Bali, K. Schilling and C. Schlichter, Phys. Rev. **D51** (1995) 5165.
- [42] M. Zach, M. Faber, W. Kainz and P. Skala, Phys. Lett. **B358** (1995) 325.
- [43] S. Chelubaraja, R.W. Haymaker and T. Matsuki, hep-lat/0210016.
- [44] G. S. Bali, B. Bolder, N. Eicker, T. Lippert, B. Orth, P. Ueberholz, K. Schilling and T. Struckmann, Phys. Rev. **D62** (2000) 054503.
- [45] C. DeTar, O. Kaczmarek, F. Karsch and E. Laermann, Phys. Rev. **D59** (1999) 031501; R.G. Edwards and U.M. Heller, Phys. Lett. **B462** (1999) 132; V. Bornyakov, Y. Nakamura, M. Chernodub, Y. Koma, Y. Mori, M. Polikarpov,

- G. Schierholz, A. Slavnov, H. Stüben and T. Suzuki, [hep-lat/0209157](#);
V. Bornyakov, H. Ichie, Y. Koma, Y. Mori, Y. Nakamura, M. Polikarpov,
G. Schierholz, T. Streuer and T. Suzuki, [hep-lat/0212023](#).
- [46] K. Schilling, Nucl. Phys. **B** (Proc. Suppl) **83** (2000) 140.
- [47] S. Kratochvila and P. de Forcrand, [hep-lat/0306011](#).
- [48] H.D.Trottier, Phys. Rev. **D60** (1999) 034506.
- [49] M. Lüscher, G. Münster and P. Weisz, Nucl. Phys. **B180** (1981) 1.
- [50] G. Bali, [hep-ph/9809351](#).
- [51] P. Olesen, Nucl. Phys. **B160** (1985) 144.
- [52] C. Bernard, T. DeGrand, C. DeTar, S. Gottlieb, U.M. Heller, J. Hetrick,
P. Lacock, K. Orginos, R.L. Sugar and D. Toussaint, Phys. Rev. **D64** (2001)
074509.
- [53] N. Arasaki, S. Ejiri, S. Kitahara, Y. Matsubara and T. Suzuki, Phys. Lett.
B395 (1997) 275.
- [54] K. Yamagishi, T. Suzuki and S. Kitahara, JHEP **02** (2000) 012.
- [55] T.L. Ivanenko, A.V. Pochinski and M.I. Polikarpov, Phys. Lett. **B252** (1990)
631.